The Astrophysical Journal, 836:24 (10pp), 2017 February 10 doi:10.3847/1538-4357/836/1/24


# JET Formation in Solar Atmosphere Due to Magnetic Reconnection

J. J. González-Avilés[1], F. S. Guzmán[1], and V. Fedun[2]
[1] Laboratorio de Inteligencia Artificial y Supercómputo, Instituto de Física y Matemáticas, Universidad Michoacana de San Nicolás de Hidalgo, Morelia, Michoacán, México
[2] Space Systems Laboratory, Department of Automatic Control and Systems Engineering, University of Sheffield, Sheffield, S1 3JD, UK
*Received 2016 September 20; revised 2016 December 16; accepted 2016 December 16; published 2017 February 6*

## Abstract

Using numerical simulations, we show that jets with features of type II spicules and cool coronal jets corresponding to temperatures of $10^4$ K can be formed as a result of magnetic reconnection in a scenario with magnetic resistivity. For this, we model the low chromosphere–corona region using the C7 equilibrium solar atmosphere model, assuming that resistive MHD rules the dynamics of the plasma. The magnetic field configurations we analyze correspond to two neighboring loops with opposite polarity. The formation of a high-speed and sharp structure depends on the separation of the loops' feet. We analyze the cases where the magnetic field strength of the two loops is equal and different. In the first case, with a symmetric configuration the jets rise vertically, whereas in an asymmetric configuration the structure shows an inclination. With a number of simulations carried out under a 2.5D approach, we explore various properties of the excited jets, namely, inclination, lifetime, and velocity. The parameter space involves a magnetic field strength between 20 and 40 G, and the resistivity is assumed to be uniform with a constant value of the order $10^{-2}\Omega \cdot m$.

*Key words:* magnetic reconnection – magnetohydrodynamics (MHD) – methods: numerical – Sun: atmosphere – Sun: magnetic fields

*Supporting material:* animations

## 1. Introduction

Magnetic reconnection is a topological reconfiguration of the magnetic field caused by changes in the connectivity of its field lines (e.g., Priest 1984, p. 171; Priest et al. 2000). It is also a mechanism of the conversion of magnetic energy into thermal and kinetic energy of plasma when two antiparallel magnetic fields encounter and reconnect with each other. Magnetic reconnection can occur in the chromosphere, photosphere, and even the convection zone. In particular, the chromosphere has a very dynamical environment where magnetic features such as $H_\alpha$ upward flow events (e.g., Chae et al. 1998) and erupting mini-filaments (e.g., Wang et al. 2000) take place. The dynamics of the chromosphere at the limb region is dominated by spicules (e.g., Beckers 1968) and related flows such as mottles and fibrils on the disk (e.g., Hansteen et al. 2006; De Pontieu et al. 2007a). Spicular structures are also visible at the limb in many spectral lines at the transition region temperatures (e.g., Mariska 1992; Wilhelm 2000), and some observations suggest that coronal dynamics are linked to spicule-like jets (e.g., McIntosh et al. 2007; De Pontieu et al. 2011; Tsiropoula et al. 2012; Skogsrud et al. 2015; Tavabi et al. 2015; Narang et al. 2016). With the large improvement in spatiotemporal stability and resolution given by the *Hinode* satellite (e.g., Kosugi et al. 2007), and with the Swedish 1 m Solar Telescope (e.g., Scharmer et al. 2008), two classes of spicules were defined in terms of their different dynamics and timescales (e.g., De Pontieu et al. 2007c).

The so-called type I spicules have lifetimes of 3–10 minutes, achieve speeds of 10–30 km $s^{-1}$, and reach heights of 2–9 Mm (e.g., Beckers 1968; Suematsu et al. 1995), and they typically involve upward motion followed by downward motion. Shibata & Suematsu (1982) and Shibata et al. (1982) studied in detail the propagating shocks using 1D models. Hansteen et al. (2006), De Pontieu et al. (2007a), and Heggland et al. (2007) studied the propagation of shocks moving upward, passing through the upper chromosphere and transition region toward the corona. They also describe how the spicule-driving shocks can be generated by a variety of processes, such as collapsing granules, *p*-modes, and dissipation of magnetic energy in the photosphere and lower chromosphere (e.g., Martínez-Sykora et al. 2009). Matsumoto & Shibata (2010) state that spicules can be driven by resonant Alfvén waves generated in the photosphere and confined in a cavity between the photosphere and the transition region. There are other papers on numerical simulations of type I spicule formation (e.g., Murawski & Zaqarashvili 2010; Murawski et al. 2011), where the authors solve the 2D ideal MHD equations and perturb the velocity field in order to stimulate the formation of type I spicules and macrospicules. Furthermore, Scullion et al. (2011) simulate the formation of the wave-driven type I spicule phenomena in 3D, the transmission of acoustic waves from the lower chromosphere to the corona, and the formation of a Transition Region Quake.

Type II spicules are observed in Ca II and H$\alpha$. These spicules have lifetimes of the order of 150 s, in contrast with type I spicules, which have lifetimes of 3–10 minutes; they are also more violent, with upward velocities of order 50–100 km $s^{-1}$, and reach greater heights. They usually only exhibit upward motion (e.g., De Pontieu et al. 2007b), followed by a fast fading in chromospheric lines without an observed downfall. Spicules of type II, which are seen in the Ca II band of *Hinode*, fade within timescales of the order of a few tenths of a second (e.g., De Pontieu et al. 2007a). The type II spicules observed on the solar disk are dubbed "Rapid Blueshifted Events" (RBEs; e.g., Langangen et al. 2008; Rouppe van der Voort et al. 2009). These show strong Doppler-blueshifted lines in the region from the middle to the upper chromosphere. The RBEs are linked with asymmetries in the transition region and coronal spectral line profiles (e.g., De Pontieu et al. 2009). In addition, the

**Table 1**
Scaling Factors to Translate Physical into Code Units

| Variable | Quantity | Unit | Value |
|---|---|---|---|
| $x, y, z$ | Length | $L_0$ | $10^6$ m |
| $\rho$ | Density | $\rho_0$ | $10^{-12}$ kg m$^{-3}$ |
| $\boldsymbol{B}$ | Magnetic field | $B_0$ | 11.21 G |
| $\boldsymbol{v}$ | Velocity | $v_0 = B_0/\sqrt{\mu_0\rho_0}$ | $10^6$ m s$^{-1}$ |
| $t$ | Time | $t_0 = L_0/v_0$ | 1 s |
| $\eta$ | Resistivity | $\eta_0 = L_0\mu_0 v_0$ | $1.25664 \times 10^6$ m$^2$ s$^{-1}$ N A$^{-2}$ |

lifetime of RBEs suggests that they are heated with at least transition region temperatures (e.g., De Pontieu et al. 2007c; Rouppe van der Voort et al. 2009). Type II spicules also show transverse motions with amplitudes of 10–30 km s$^{-1}$ and periods of 100–500 s (e.g., Tomczyk et al. 2007; McIntosh et al. 2011; Zaqarashvili & Erdélyi 2009), which are interpreted as upward- or downward-propagating Alfvénic waves (e.g., Okamoto & De Pontieu 2011; Tavabi et al. 2015b) or MHD kink mode waves (e.g., He et al. 2009; McLaughlin et al. 2012; Kuridze et al. 2012).

As mentioned above, there are several theoretical and observational results with regard to type II spicules, but there is little consensus about the origin of type II spicules and the source of their transverse oscillations. Some possibilities discussed suggest that type II spicules are due to the magnetic reconnection process (e.g., Isobe et al. 2008; De Pontieu et al. 2007c; Archontis et al. 2010), oscillatory reconnection process (e.g., Heggland et al. 2009; McLaughlin et al. 2012), strong Lorentz force (e.g., Martínez-Sykora et al. 2011), Lorentz force under chromospheric conditions (e.g., Goodman 2012), or propagation of $p$-modes (e.g., de Wijn et al. 2009). Moreover, type II spicules could be warps in 2D sheet-like structures (e.g., Judge et al. 2011). More recently, Sterling & Moore (2016) suggest another mechanism in which solar spicules result from the eruptions of small-scale chromospheric filaments.

The limited resolution in observations and the complexity of the chromosphere make the interpretation of the structures difficult, even calling into question the existence of type II spicules as a particular class (e.g., Zhang et al. 2012). In consequence, these difficulties spoil the potential importance of magnetic reconnection as a transcendent mechanism in the solar surface. Nevertheless, there is evidence that magnetic reconnection is a good explanation for chromospheric anemone jets (e.g., Singh et al. 2012), which are observed to be much smaller and much more frequent than surges (e.g., Shibata et al. 2007). A statistical study performed by Nishizuka et al. (2011) showed that the chromospheric anemone jets have typical lengths of 1.0–4.0 Mm, widths of 100–400 km, and cusp sizes of 700–2000 km. Their lifetime is about 100–500 s, and their velocity is about 5–20 km s$^{-1}$. Other types of coronal jets can be generated by magnetic reconnection; for example, Yokoyama & Shibata (1995, 1996) used 2D numerical simulations to study the jet formation, and Nishizuka et al. (2008) showed that emerging magnetic flux reconnects with an open ambient magnetic field and that such reconnection produces the acceleration of material and thus a jet structure. The reconnection seems to trigger the jet formation in a horizontally magnetized atmosphere, with the flux emergence as a mechanism (e.g., Archontis et al. 2005; Galsgaard et al. 2007).

Another approach uses a process that produces a magnetic reconnection using numerical dissipation of the ideal MHD equations, and the atmosphere model is limited to having constant density and pressure profiles and assumes that there is no gravity (e.g., Pariat et al. 2009, 2010, 2015; Rachmeler et al. (2010). In our case we show that magnetic reconnection can be responsible for the formation of jets with some characteristics of type II spicules and cold coronal jets (e.g., Nishizuka et al. 2008), for that (i) we solve the system of equations of the resistive MHD subject to the solar gravitational field, and (ii) we assume a completely ionized solar atmosphere consistent with the C7 model. The resulting magnetic reconnection accelerates the plasma upward by itself and produces the jet.

The paper is organized as follows. In Section 2 we describe the resistive MHD equations, the model of solar atmosphere, the magnetic field configuration used in the numerical simulations, and the numerical methods we use. In Section 3 we present the results of the numerical simulations for various experiments. Section 4 contains final comments and conclusions.

## 2. Model and Numerical Methods

### 2.1. The System of Resistive MHD Equations

The system of equations allowing the formation of magnetic reconnection is the resistive MHD. In this paper we follow Jiang et al. (2012) to write the dimensionless Extended Generalized Lagrange Multiplier (EGLM) resistive MHD equations that include gravity as follows:

$$\frac{\partial \rho}{\partial t} + \nabla \cdot (\rho \boldsymbol{v}) = 0, \tag{1}$$

$$\frac{\partial (\rho \boldsymbol{v})}{\partial t} + \nabla \cdot \left( \left( p + \frac{1}{2}\boldsymbol{B}^2 \right) \boldsymbol{I} + \rho \boldsymbol{v}\boldsymbol{v} - \boldsymbol{B}\boldsymbol{B} \right) = -(\nabla \cdot \boldsymbol{B})\boldsymbol{B} + \rho \boldsymbol{g}, \tag{2}$$

$$\frac{\partial E}{\partial t} + \nabla \cdot \left( \boldsymbol{v}\left( E + \frac{1}{2}\boldsymbol{B}^2 + p \right) - \boldsymbol{B}(\boldsymbol{B} \cdot \boldsymbol{v}) \right) = -\boldsymbol{B} \cdot (\nabla \psi) - \nabla \cdot ((\eta \cdot \boldsymbol{J}) \times \boldsymbol{B}) + \rho \boldsymbol{g} \cdot \boldsymbol{v}, \tag{3}$$

$$\frac{\partial \boldsymbol{B}}{\partial t} + \nabla \cdot (\boldsymbol{B}\boldsymbol{v} - \boldsymbol{v}\boldsymbol{B} + \psi \boldsymbol{I}) = -\nabla \times (\eta \cdot \boldsymbol{J}), \tag{4}$$

$$\frac{\partial \psi}{\partial t} + c_h^2 \nabla \cdot \boldsymbol{B} = -\frac{c_h^2}{c_p^2}\psi, \tag{5}$$

$$\boldsymbol{J} = \nabla \times \boldsymbol{B},$$

$$E = \frac{p}{(\gamma - 1)} + \frac{\rho \boldsymbol{v}^2}{2} + \frac{\boldsymbol{B}^2}{2},$$

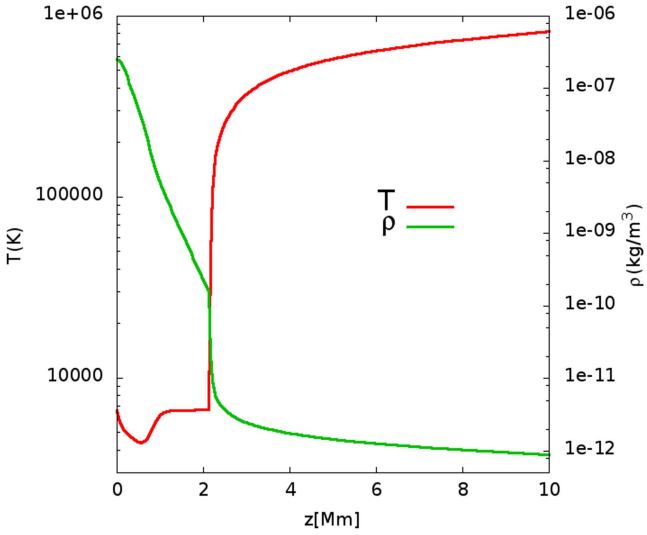


**Figure 1.** Temperature (red) and mass density (green) as a function of height for the C7 equilibrium solar atmosphere model. Notice the steep jump in temperature.

where $\rho$ is the mass density, $\boldsymbol{v}$ is the velocity vector field, $\boldsymbol{B}$ is the magnetic vector field, $E$ is the total energy density, where $\gamma = 5/3$, the plasma pressure $p$ is described by the equation of state of an ideal gas, $\boldsymbol{g}$ is the gravitational field, $\boldsymbol{J}$ is the current density, $\eta$ is the magnetic resistivity tensor, and $\psi$ is a scalar potential that helps damp out the violation of the constraint $\nabla \cdot \boldsymbol{B} = 0$. Here $c_h$ is the wave speed and $c_p$ is the damping rate of the wave of the characteristic mode associated with $\psi$. In this study we consider uniform and constant magnetic resistivity, because the solar chromosphere is fully collisional and anomalous or space-dependent resistivity—which is the result of various collisionless processes—may not be expected (e.g., Singh et al. 2011). We normalize the equations with the quantities given in Table 1, which are typical scales in the solar corona.

In the EGLM-MHD formulation, Equation (5) is the magnetic field divergence free constraint. As suggested in Dedner et al. (2002), the expressions for $c_h$ and $c_p$ are

$$c_h = \frac{c_{cfl}}{\Delta t}\min(\Delta x, \Delta y, \Delta z), \quad c_p = \sqrt{-\Delta t \frac{c_h^2}{\ln c_d}},$$

where $\Delta t$ is the time step, $\Delta x$, $\Delta y$, and $\Delta z$ are the spatial resolutions, $c_{cfl} < 1$ is the Courant factor, and $c_d$ is a problem-dependent coefficient between 0 and 1; this constant determines the damping rate of divergence errors. The parameters $c_h$ and $c_p$ are not independent of the grid resolution and the numerical scheme used; for that reason one should adjust their values. In our simulations we use $c_p = \sqrt{c_r}\, c_h$, with $c_r = 0.18$ and $c_h = 0.01$. For our analysis we use a 2.5D model, which means that all the state variables depend on $x$ and $z$, where $x$ is a horizontal coordinate and $z$ labels height, and a nonzero component of the vector field $v_y$ and a nontrivial magnetic field $y$-component $B_y$ that vary with $x$ and $z$ are allowed (e.g., González-Avilés & Guzmán 2015; González-Avilés et al. 2015). In this work we solve the 2.5D version of the resistive MHD equations on the $xz$ plane with resolution $\Delta x$ and $\Delta z$.

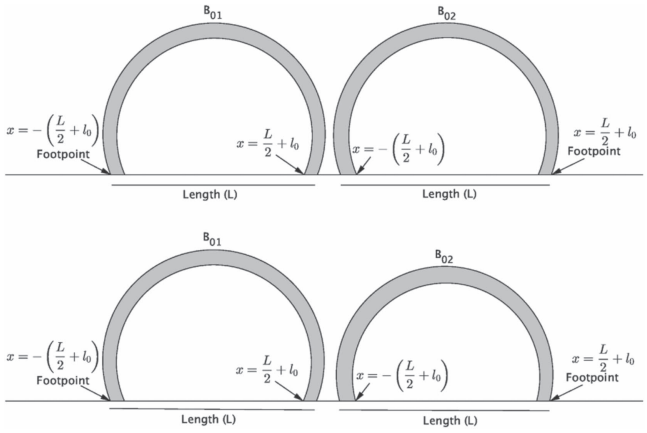


**Figure 2.** Top: two consecutive symmetric magnetic loop configurations with the same field strength $B_{01} = B_{02}$. Bottom: two consecutive nonsymmetric magnetic loop configurations for the case $B_{01} > B_{02}$. The length of each loop is represented by $L$, and the location of footpoints is determined by the parameter $l_0$.

### 2.2. Numerical Methods

We solve numerically the resistive EGLM-MHD equations given by the system of Equations (1)–(5) on a single uniform cell centered grid, using the method of lines with a third-order total variation diminishing Runge–Kutta time integrator (e.g., Shu & Osher 1989). In order to use the method of lines, the right-hand sides of resistive MHD equations are discretized using a finite volume approximation with high-resolution shock-capturing methods (e.g., LeVeque 1992). For this, we first reconstruct the variables at cell interfaces using the Minmod limiter. Numerical fluxes are calculated using the Harten–Lax–van Leer–Contact approximate Riemann solver (e.g., Li 2005).

### 2.3. Model of the Solar Atmosphere

We choose the numerical domain to cover part of the photosphere, chromosphere, and corona. We consider the atmosphere in the hydrostatic equilibrium and study the evolution on a finite $xz$ domain. The temperature field is assumed to obey the semiempirical C7 model of the chromosphere-transition region (e.g., Avrett & Loeser 2008) and is distributed to obtain the optimum agreement between calculated and observed continuum intensities, line intensities, and line profiles of the SUMER (e.g., Curdt et al. 1999) atlas of the extreme-ultraviolet (EUV) spectrum. The model includes the photosphere as presented in Fontela et al. (1990) and is extended to the solar corona, as is described by Griffiths et al. (1999). The profiles of $T(z)$ and $\rho(z)$ are shown in Figure 1, where the expected gradients at the transition region can be seen.

### 2.4. The Magnetic Field

The magnetic field in the model is chosen as a superposition of two neighboring loops. The idea behind this type of configuration is that the magnetic field of the two loops has a different polarity in the region where they are close to each other. This kind of configuration has been observed to trigger solar flares, as reported in Takasao et al. (2012) and Su et al. (2013), where through EUV and X-ray data the reconnection was observed, as inflowing cool loops and outflowing hot

**Table 2**
Maximum Height, Vertical Velocity, Temperature, Density, and Time When the Jets Reach the Maximum Height for Each Magnetic Field Configuration

| Run # | $B_{01}$ (G) | $B_{02}$ (G) | $l_0$ (Mm) | $h_{\max}$(Mm) | $v_{z,h_{\max}}$ (km s$^{-1}$) | $T_{\mathrm{inside},h_{\max}}$ (K) | $\rho_{\mathrm{inside},h_{\max}}$ (kg m$^{-3}$) | $t_{h_{\max}}$ (s) |
|---|---|---|---|---|---|---|---|---|
| 1 | 40 | 40 | 3.5 | 7.3 | 15.4 | 14200 | $1.32 \times 10^{-10}$ | 210.2 |
| 2 | 30 | 30 | 2.5 | 2.3 | 33.9 | 48452 | $2.5 \times 10^{-10}$ | 70.4 |
| 3 | 30 | 30 | 3.5 | 3.9 | 13.4 | 22532 | $1.3 \times 10^{-10}$ | 196.8 |
| 4 | 20 | 20 | 2.5 | 1.5 | 12.1 | 25933 | $1.2 \times 10^{-10}$ | 94.4 |
| 5 | 20 | 20 | 3.0 | 1.8 | 3.7 | 47990 | $1.0 \times 10^{-10}$ | 142.4 |
| 6 | 20 | 20 | 3.5 | 1.2 | 8.7 | 27334 | $1.4 \times 10^{-10}$ | 160 |
| 7 | 40 | 30 | 3.5 | 7.2 | 16.8 | 34112 | $4.0 \times 10^{-11}$ | 213.3 |
| 8 | 40 | 20 | 3.0 | 1.2 | 76.5 | 76467 | $1.0 \times 10^{-9}$ | 11.2 |
| 9 | 40 | 20 | 3.5 | 6.7 | 31.0 | 110560 | $1.2 \times 10^{-11}$ | 211.2 |
| 10 | 30 | 20 | 2.5 | 2.8 | 61.4 | 30565 | $6.4 \times 10^{-10}$ | 52.8 |
| 11 | 30 | 20 | 3.0 | 2.7 | 11.0 | 31201 | $8.6 \times 10^{-11}$ | 139.2 |
| 12 | 30 | 20 | 3.5 | 3.1 | 5.8 | 31931 | $5.8 \times 10^{-11}$ | 204.8 |

**Note.** We include symmetric ($B_{01} = B_{02}$) and nonsymmetric ($B_{01} \neq B_{02}$) cases.

loops. Inspired by this, we set a similar magnetic field topology with a weaker strength. Following Priest (1982) and Del Zanna et al. (2005), we construct a loop with the vector potential

$$A_y(x, z) = \frac{B_{01}}{k}\cos(kx)\exp(-kz), \quad (6)$$

where $B_{01}$ is the photospheric field magnitude at the footpoints $x = \pm L/2$ and $k = \pi/L$. Here $L$ is the distance between the two footpoints of the loop, and $k$ defines the nodes of the potential. In this model the components of the magnetic field are represented as

$$B_x(x, z) = B_{01}\cos(kx)\exp(-kz), \quad (7)$$

$$B_z(x, z) = -B_{01}\sin(kx)\exp(-kz). \quad (8)$$

In order to superpose two loops, we use a modified version of Equation (6):

$$A_y(x, z) = \frac{B_{01}}{k}\cos(k(x + l_0))\exp(-kz) + \frac{B_{02}}{k}\cos(k(x - l_0))\exp(-kz), \quad (9)$$

where $l_0$ defines the location of the footpoints for each loop, and $B_{01}$ and $B_{02}$ are the magnetic field strengths of the left and right loop, respectively. With the parameter $l_0$ it is possible to control the separation between the two magnetic loops, which in turn will influence the thickness of a current sheet. The case $B_{01} = B_{02}$ describes two neighboring loop configurations with the same magnetic field strength, whereas $B_{01} \neq B_{02}$ describes two nearby loops with different magnetic field strengths. A schematic picture of these two configurations is shown in Figure 2.

## 3. Results of Numerical Simulations

The numerical integration with high-resolution shock-capturing methods introduces a problem and resolution-dependent numerical dissipation, which may account for important effects, including magnetic reconnection. For instance, in Pariat et al. (2009, 2010, 2015) numerical dissipation is used to emulate resistivity. In our case we solve the resistive MHD equations to account for the physical and not the numerical effect of resistivity. We ran a number of simulations with the magnetic field configuration given by Equation (9) in a scenario with constant resistivity $\eta = 5 \times 10^{-2}\ \Omega \cdot m$ across the whole domain, which is a realistic value estimated for a fully ionized solar atmosphere (e.g., Priest 2014). We verified that when the resistivity is set to zero no jet formation was observed in all the cases. This indicates that the magnetic reconnection is not due to the numerical methods. We experimented with various values of the magnetic field strength and separation of the loops, as indicated in Table 2.

We fixed $k = \pi/L$ with $L = 8$ Mm, and the simulations were carried out in a domain $x \in [-4, 4]$, $y \in [0, 1]$, $z \in [0, 10]$ in units of Mm, covered with $300 \times 4 \times 375$ grid cells. In all the numerical simulations we used outflow boundary conditions, which in our approach translates into $(\nabla f) \cdot \hat{n} = 0$, where $f$ is any of our conservative variables and $\hat{n}$ is a unit normal vector to each of the faces of the domain (e.g., Toro 2009). These boundary conditions are appropriate for this problem because they behave as stationary as long as no flux is approaching the boundaries, and as soon as any mode reaches the boundaries, it is free to get off the domain.

We study the formation of structures considering various scenarios. The magnetic field parameters of the simulations we study in this paper are summarized in Table 2.

### 3.1. Symmetric Configurations

We show the results for the case $B_{01} = B_{02}$ for three values of magnetic strength: 20, 30, 40 G and $l_0 =$ 2.5, 3.0, 3.5 Mm. Representative simulations for this case are shown in Figure 3 for $l_0 = 3.5$ Mm. Run #1 corresponds to the typical formation of a jet, with a special feature at the top with a bulb possibly related to the formation of a Kelvin–Helmholtz (KH) type of instability. This jet reaches a maximum height of 7.3 Mm, which we denote by $h_{\max}$ in this and the cases below. The speed of the jet (evaluated at $h_{\max}$) is $v_{z,h_{\max}} \approx 15.4$ km s$^{-1}$; unlike other analyses (e.g., Heggland et al. 2007), where the maximum speed refers to the whole domain, we measure the speed at $h_{\max}$ in order to avoid the possibility that the maximum speed happens at the base of the jet instead of at the top. This maximum height is achieved at time $t_{h_{\max}} = 210.2$ s. After this time, the jet starts to fall down until it disperses away by time $t \approx 400$ s. An animation of Run #1 is presented in the online version of Figure 4. In the top of Figure 5 we show the temperature and velocity inside the jet, $T_{\mathrm{inside}}$ and $v_{z,\mathrm{inside}}$, as a function of time, where the subscript "inside" means that they are measured inside the head of the jet on the fly. We show in Figure 3 the magnitude of the current density $|\boldsymbol{J}|$, which shows the formation of an elongated structure consistent with the

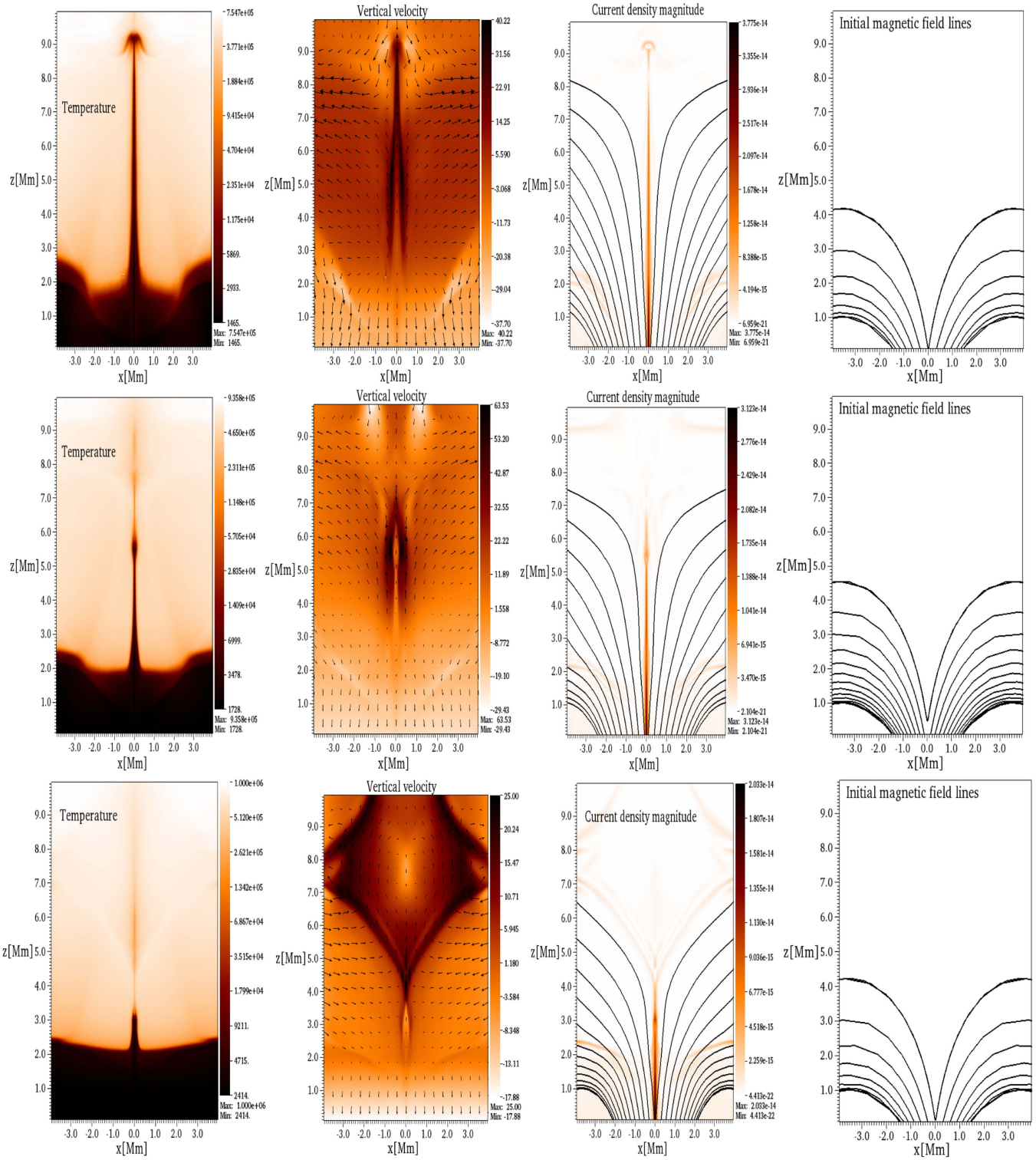


**Figure 3.** From left to right we show snapshots of (i) logarithm of the temperature in kelvin; (ii) the vertical component of the velocity ($v_z$ km s$^{-1}$), where the arrows show the velocity field distribution; (iii) the magnitude of the current density $|\boldsymbol{J}|$ (A m$^{-2}$); and (iv) the magnetic field configuration at the initial time, which helps us notice the distortions of the field during the evolution. In the top panels we show the results for Run #1, where $B_{01} = B_{02} = 40$ G at time $t = 210.136$ s. In the middle panels we present the results for Run #3, where $B_{01} = B_{02} = 30$ G at time $t = 196.8$ s. Finally, in the bottom panels we show the results for Run #6, where $B_{01} = B_{02} = 20$ G at time $t = 160$ s. In all the cases $l_0 = 3.5$ Mm.

reconnection process and has its maximum in a zone right below the transition region in the three cases where beta $\beta > 1$.

In the middle panels of Figure 3 we show the results for Run #3. Since the magnetic field is weak, the resulting jet reaches a maximum height of 3.9 Mm with a vertical velocity $v_{z,h_{\max}} \approx 13.4$ km s$^{-1}$ at time $t = 196.8$ s. Finally, in the bottom panels of Figure 3, we show Run #6; in this case the effect of an even weaker magnetic field is seen in the appearance of a small jet that reaches a maximum height of 1.2 Mm with a speed $v_{z,h_{\max}} \approx 8.7$ km s$^{-1}$ at time $t = 160$ s.

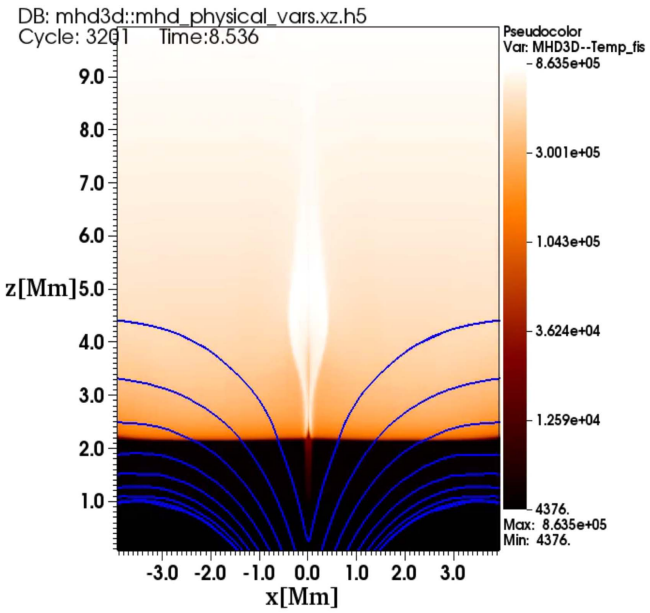


**Figure 4.** Online animation showing the evolution of the logarithm of the temperature (colored heat map) in kelvin with the magnetic field lines (colored in blue) for Run #1, where $B_{01} = B_{02} = 40$ G and $l_0 = 3.5$ Mm. The 15 s video spans an approximately 400 s duration jet. In this animation we can see that the jet appears at the transition region and starts to move straight upward until reaching a maximum height at approximately $t = 210$ s; after this time, the jet starts to disperse and disappear at about $t = 400$ s. The magnetic field lines show a symmetric distortion due to the straight motion of the jet.

(An animation of this figure is available.)

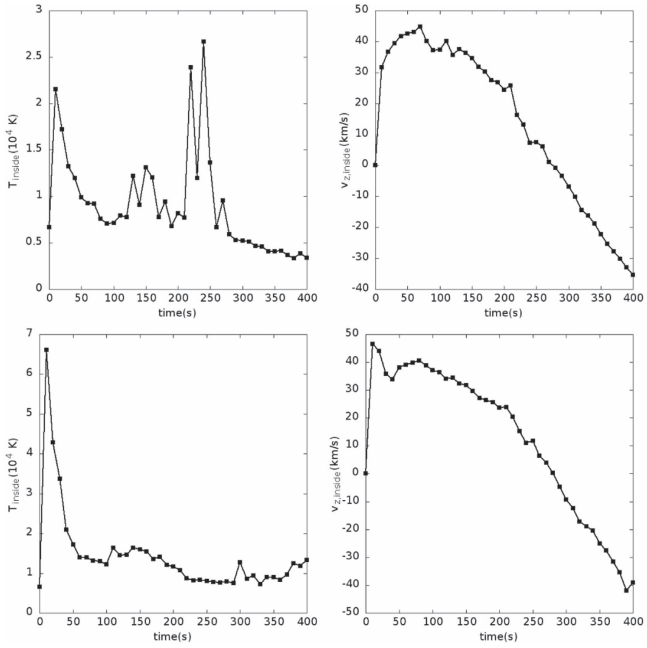


**Figure 5.** Some properties of the jet using diagnostics of the temperature of the jet $T_{\rm inside}$ and the vertical velocity $v_{z,\rm inside}$ as a function of time. We estimate these quantities every 10 s. Top: the case $B_{01} = B_{02} = 40$ G and $l_0 = 3.5$ Mm. From the velocity data we can see that the jet starts to disperse at $t \approx 200$ s. Bottom: the case $B_{01} = 40$, $B_{02} = 30$ G, and $l_0 = 3.5$ Mm; in this case the jet starts to disperse away also at $t \approx 200$ s.

These results indicate that the height of the jet is larger for higher values of $B_{01} = B_{02}$, and the sharpness of the jet is also clearer for strong magnetic fields.

The separation of the loops determines the formation of the jets. In the case of configurations with a larger separation, the plasma is accelerated rapidly, which produces diffusion, and consequently the jet does not form. However, in the case of closer loops, the plasma is accelerated slowly, which allows the formation of a jet later on. According to our results, for the parameters we analyzed, the most effective value of $l_0$ to trigger a jet is $l_0 = 3.5$ Mm.

### 3.2. Nonsymmetric Configurations

In this case we show the results for a less idealized magnetic field configuration where the magnetic field loops have different strengths ($B_{01} \neq B_{02}$) for the combinations of magnetic field strengths 20, 30, and 40 G and $l_0 =$ 2.5, 3.0, 3.5 Mm. In order to illustrate the effect of the asymmetry in the formation of jets, we show the results for Runs #7, #9, and #12 in Figure 6. In the top panels we present the result for Run #7, which shows the inclination of the jet toward the loop with the weak magnetic field. Similar to the previous case, the top part of the jet exhibits a bulb similar to a KH instability (e.g., Kuridze et al. 2016). This jet reaches a maximum height of 7.2 Mm and a vertical velocity $v_{z,h_{\rm max}} \approx 16.8\,{\rm km\,s^{-1}}$ at $t = 213.3$ s. Like in the symmetric case, the jet starts to weaken and finally vanishes, which can be seen in the bottom panels of Figure 5 in the time domain. An animation of Run #7 is presented in the online version of Figure 7. Also in Figure 5 we show $T_{\rm inside}$ and $v_{z,\rm inside}$ as a function of time estimated inside the jet for Run #7. In the middle panels of Figure 6 we show Run #9, and in this case the jet shows a more significant inclination. The jet reaches a maximum height of 6.7 Mm and vertical velocity $v_{z,h_{\rm max}} \approx 31\,{\rm km\,s^{-1}}$ at time $t = 211.2$ s. The inclination is also shown in the magnitude of current density $|\boldsymbol{J}|$. In the bottom panels we show Run #12, where the jet is small, due to the weaker magnetic field of the loops. The maximum height of the jet is about 3.1 Mm, and its vertical velocity is $v_{z,h_{\rm max}} \approx 5.8\,{\rm km\,s^{-1}}$ at $t = 204.8$ s.

The velocity vector field shows that the plasma moves toward the loop with weaker magnetic field strength. One can appreciate some geometrical resemblance on the magnitude of the current density $|\boldsymbol{J}|$ maps from the simulations, with the intensity maps in Ca II Ha emission lines seen in the observations with *Hinode*/SOT (see Figure 1 of Tavabi et al. 2015b). We do not show the density of the plasma in these figures, because its shape is pretty much that of the temperature profile.

We summarize the diagnostic results for all the combinations of the magnetic field configurations in Table 2. These are the maximum height $h_{\rm max}$, the velocity of the plasma along the vertical direction $v_{z,h_{\rm max}}$, the plasma temperature $T_{\rm inside}$ measured at $h_{\rm max}$, density $\rho_{\rm inside}$ also measured at maximum height, and time when the jets reach the maximum height $t_{h_{\rm max}}$.

In the case of nonsymmetric magnetic loops, the inclination depends on the magnetic field strength between the two loops, as shown in Figure 6. In order to see this dependence more clearly, we show the inclination angle of the jet as a function of the ratio $B_{02}/B_{01}$ for different separation parameters in Figure 8 at the time when the jet reaches the maximum height for each case.

We were wondering whether the bulb appearing at the top of the jet is due to a KH instability taking place during the evolution of the jet. For this we monitor the condition

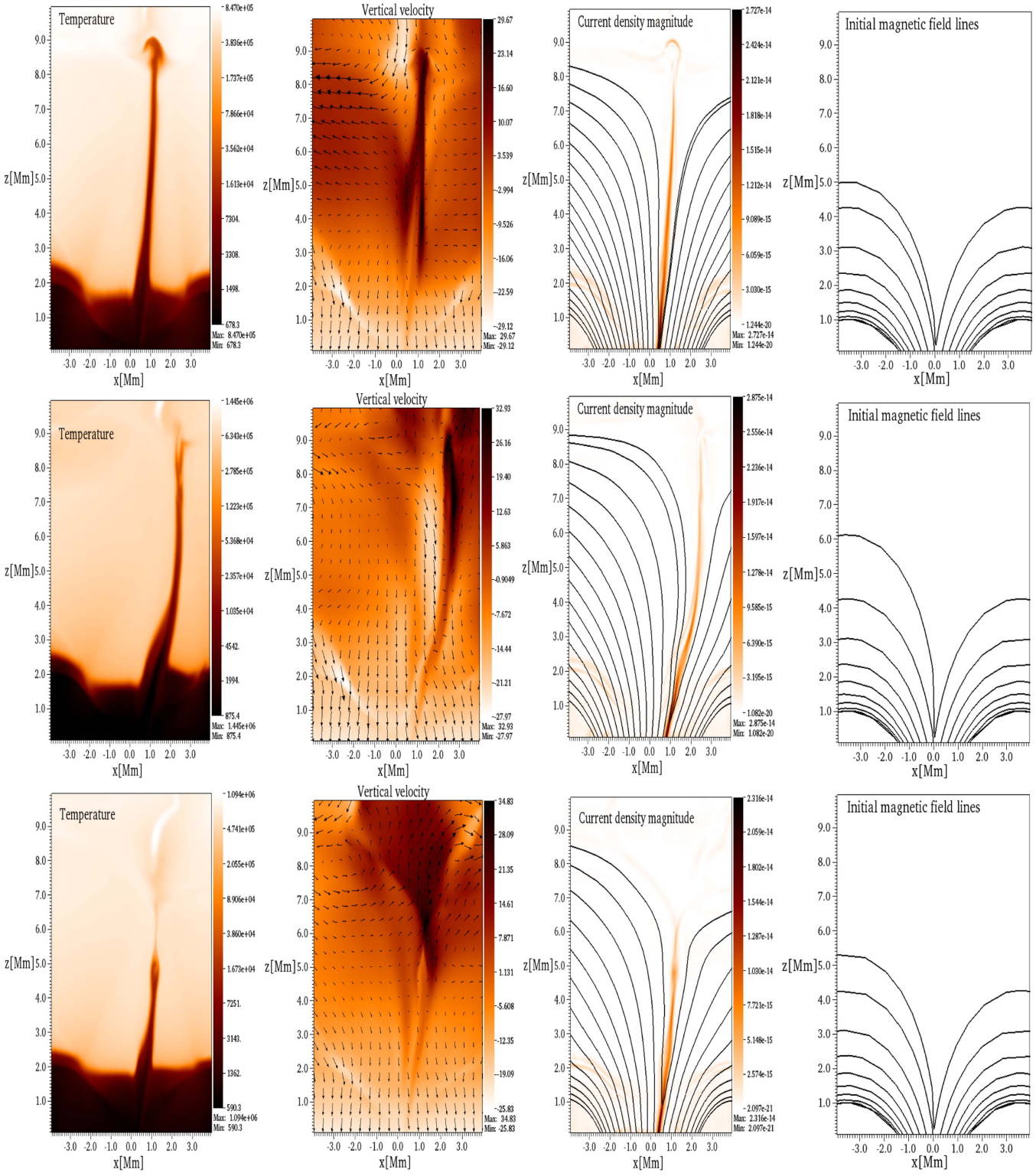


**Figure 6.** From left to right we show snapshots of (i) logarithm of the temperature in kelvin; (ii) the vertical component of the velocity ($v_z$ km s$^{-1}$) in color with the velocity vector field; (iii) the magnitude of the current density $|\boldsymbol{J}|$ (A m$^{-2}$) at the time when the jet reaches the maximum height; and (iv) the magnetic field configuration at initial time. In the top panels we show the results for Run #7, where $B_{01} = 40$, $B_{02} = 30$ G at time $t = 213.3$ s. In the middle panels we present the results for Run #9, where $B_{01} = 40$, $B_{02} = 20$ G at time $t = 211.2$ s. Finally, in the bottom panels we show the results for Run #13, where $B_{01} = 30$, $B_{02} = 20$ G at time $t = 204.8$ s. In all the cases $l_0 = 3.5$ Mm.

(Chandrasekhar 1961; Cowling 1976)

$$\frac{B_z^{(-)^2} + B_z^{(+)^2}}{\mu_0 \rho^{(+)} \rho^{(-)}} (\rho^{(+)} + \rho^{(-)}) \geqslant (v_z^{(-)} - v_z^{(+)})^2, \qquad (10)$$

where $B_z^{(-)}$ and $B_z^{(+)}$ represent the vertical magnetic field outside and inside the jet, respectively. Here $\rho^{(-)}$ and $\rho^{(+)}$ are the corresponding values of the mass density, $\mu_0$ is the magnetic permeability, and $v_z^{(-)}$ and $v_z^{(+)}$ are the vertical components of the

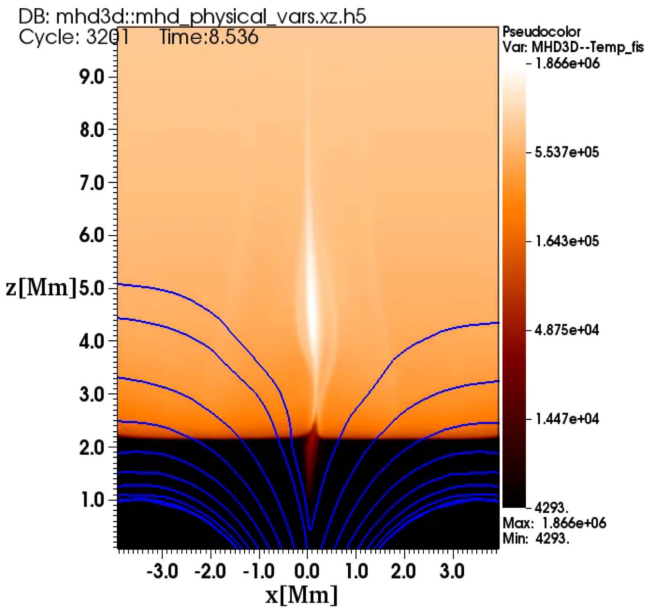


**Figure 7.** Online animation showing the evolution of the logarithm of the temperature (colored heat map) in kelvin with the magnetic field lines (colored in blue) for Run #7, where $B_{01} = 40$, $B_{02} = 30$ G and $l_0 = 3.5$ Mm. The 15 s video spans an approximately 400 s duration jet. In this animation we can see that the jet appears at the transition region and starts to move upward with an inclination with respect to the loop with weaker magnetic field strength. This jet reaches a maximum height at approximately $t = 213$ s; after this time, the jet starts to disperse and disappear at about $t = 400$ s, similar to the animation of Run #1. In this case the magnetic field lines show a clear distortion due to the evolution of the jet into a nonsymmetric magnetic field loop configuration.

(An animation of this figure is available.)

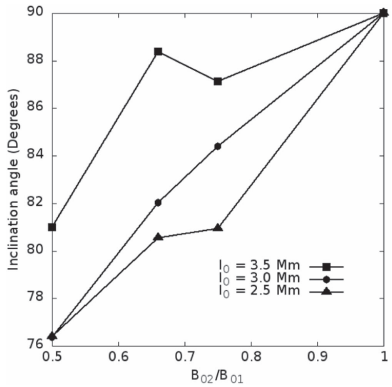


**Figure 8.** Inclination angle of the jet measured when it reaches the maximum height as a function of the ratio $B_{02}/B_{01}$ for the cases of two nonsymmetric magnetic loops with separations $l_0 = 3.5$, 3.0, 2.5 Mm.

velocity. Condition (10) implies that if the magnetic field is parallel to the jet, such a perturbation stretches the field lines and produces a restoring force when the magnetic fields are strong enough to suppress the instability if the condition given by Equation (10) is satisfied.

We measure the quantities involved in Equation (10) in two places and two different times in order to track any possible violation of this condition. For this we choose Run #1 and check whether or not Equation (10) is satisfied at times $t_1 = 100$ s, when the jet is still moving upward and possibly causes a KH instability, and at $t_2 = 210$ s, which is the time near its maximum height, when the bulb is already formed. The measurements are presented in Table 3. We found that at $t = t_1$ the inequality is verified by nearly an order of magnitude, whereas at $t = t_2$, at the top of the bulb, when the jet is almost at rest, the inequality is barely satisfied, which implies that the KH instability tends to appear but is suppressed by the magnetic field. Nevertheless, at the bottom of the jet the inequality is nearly satisfied and we cannot see any feature of a KH instability.

According to the parameters of Table 3 for both examples, the condition given by Equation (10) is satisfied, which implies that magnetic field should suppress the KH instability.

## 4. Conclusions

In this paper we present the numerical solution of the equations of the resistive MHD submitted to the solar constant gravitational field and simulate the formation of narrow jet structures on the interface low chromosphere and corona. For this we use a magnetic field configuration of two superposed loops that allows the magnetic reconnection process, which in turn accelerates the plasma. Our model is idealized in the sense that it needs a region with mixed polarity nearby, even though many type II spicules are observed in regions where the magnetic field is predominantly unipolar.

An ingredient of our simulations is that we use an atmospheric model that includes the transition region, and the rarefied environment above the transition region helps the acceleration of the plasma. We can summarize our findings in the schematic picture shown in Figure 9. This rarefied atmosphere allows the formation of a bulb at the top of the jet, which would be interesting if it were due to a KH instability (e.g., Kuridze et al. 2016), contained and stabilized by the magnetic field as found in Flint et al. (2014) and Zaqarashvili et al. (2014). However, we found that the conditions under the approximate approach of Equation (10) are not sufficient for a KH instability to hold, although it is only an idealized approximation and there is still a chance that a KH process happens.

We consider symmetric and asymmetric magnetic field configurations. In the symmetric case, different jet properties were found in terms of separation and the magnetic field strength of the loops. The magnetic field used ranges from 20 to 40 G, leading to the conclusion that the stronger the magnetic field, the higher the jet. The temperature within the jet structure is of the order of $10^4$ K in all the cases, which is within the observed range of a cool jet (e.g., Nishizuka et al. 2008). An illustrative example is that of $B_{01} = B_{02} = 40$ G and $l_0 = 3.5$ Mm, which shows a maximum height of 7.3 Mm measured from the transition region and a vertical velocity of $v_{z,h_{\max}} \approx 15.4$ km s$^{-1}$. Our simulations indicate that the jets may last for about 200 s, which is slightly above the 50–150 s for observed type II spicules (e.g., De Pontieu et al. 2007c), whereas the velocity of our jets lies in the lower bound of the observations.

In the case of asymmetric magnetic field configurations we also simulated the formation of jets with similar properties of temperature, velocity, lifetime, and height of the symmetric configurations. The main feature is that jets show a considerable inclination toward the loop with the weaker magnetic field. We found that the inclination of the jet depends on the magnetic field ratio of the two loops.

According to the results of this paper, a good model for the formation of jets mimicking some properties of cool coronal jets (Nishizuka et al. 2008) and type II spicules is to have two

**Table 3**
Measured Parameters Related to Condition (10)

| Case | $\rho^{(+)}$ (kg m$^{-3}$) | $\rho^{(-)}$ (kg m$^{-3}$) | $v_z^{(+)}$ (km s$^{-1}$) | $v_z^{(-)}$ (km s$^{-1}$) | $B_z^{(+)}$ (T) | $B_z^{(-)}$ (T) | Time (s) |
|---|---|---|---|---|---|---|---|
| Example 1 (bottom of the jet) | $2.27 \times 10^{-9}$ | $2.96 \times 10^{-10}$ | 7.54 | 1.35 | $5.6 \times 10^{-4}$ | $1.94 \times 10^{-3}$ | 100.3 |
| Top of the jet | $1.66 \times 10^{-10}$ | $2.06 \times 10^{-12}$ | 38.86 | 25.27 | $2.83 \times 10^{-4}$ | $3.99 \times 10^{-4}$ | 100.3 |
| Example 2 (bottom of the jet) | $1.057 \times 10^{-9}$ | $3.57 \times 10^{-11}$ | −5.85 | −7.07 | $4.39 \times 10^{-4}$ | $1.33 \times 10^{-3}$ | 210.2 |
| Top of the jet | $1.40 \times 10^{-10}$ | $7.12 \times 10^{-12}$ | 15.4 | −4.60 | $-3.056 \times 10^{-5}$ | $-2.7 \times 10^{-4}$ | 210.2 |

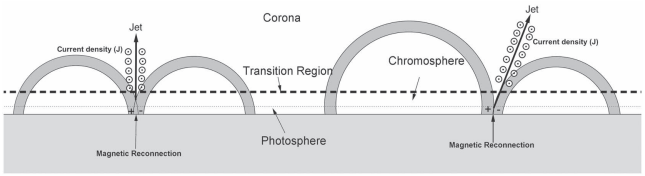


**Figure 9.** Two configurations of the magnetic coronal loops with footpoints at the photospheric level. Initially two magnetic loops close together have opposite polarity, which produces magnetic reconnection. In the case of two symmetric magnetic loops (left) the jet appears at the middle of the configuration and moves straight upward until it reaches the solar corona and diffuses later on. In the case of two asymmetric loops (right) the jets are formed and evolve at the middle of the configuration, but in this case the loop with the stronger magnetic field pushes the jet toward the loop with the weak magnetic field. In both cases there is an elongated structure represented by the density current $J$ in the perpendicular direction to the jet.

magnetic loops close together with opposite polarity. This produces magnetic reconnection, which accelerates the plasma. A key ingredient in the process is the inclusion of magnetic resistivity, which is a mechanism consistent with the magnetic reconnection process.

This research is partly supported by the following grants: Newton Fund—MAS/CONACyT Mobility Grants Program, Royal Society-Newton Mobility Grant NI160149, CIC-UMSNH 4.9, and CONACyT 258726 (Fondo Sectorial de Investigación para la Educación). V.F. would like to thank the STFC for their financial support. The simulations were carried out in the IFM Draco cluster funded by CONACyT 106466 and in the Sciesmex cluster at IG-UNAM.

## References

Archontis, V., Moreno-Insertis, F., Galsgaard, K., & Hood, A. W. 2005, ApJ, 635, 1299
Archontis, V., Tsinganos, K., & Gontikakis, C. 2010, A&A, 512, L2
Avrett, E. H., & Loeser, R. 2008, ApJS, 175, 229
Beckers, J. M. 1968, SoPh, 3, 367
Chae, J., Wang, H., Lee, C., Goode, P. R., & Schulhe, U. 1998, ApJL, 504, L123
Chandrasekhar, S. 1961, Hydrodynamic and Hydromagnetic Stability (Oxford: Clarendon) Chapter 11
Cowling, T. K. 1976, Magnetohydrodynamics (Bristol: Hilger)
Curdt, W., Heinzel, P., Schmidt, W., et al. 1999, in ESA SP-448, ed. A. Wilson (Noordwijk: ESA), 177
Dedner, A., Kemm, F., Kroner, D., et al. 2002, JCoPh, 175, 645
Del Zanna, L., Schaekens, E., & Velli, M. 2005, A&A, 431, 1095
De Pontieu, B., Hansteen, V. H., Rouppe van der Voort, L., van Noort, M., & Carlsson, M. 2007a, ApJ, 655, 624
De Pontieu, B., McIntosh, S. W., Hansteen, V., & Carlsson, M. P. 2007b, in AGU Fall Meeting Abstracts, #SH52C-08
De Pontieu, B., McIntosh, S. W., Hansteen, V. H., & Schrijver, C. J. 2009, ApJL, 701, L1
De Pontieu, B., McIntosh, S., Hansteen, V. H., et al. 2007c, PASJ, 59, 655
De Pontieu, B., McIntosh, S., Carlsson, M., et al. 2011, Sci, 331, 55
de Wijn, A. G., McIntosh, S. W., & De Pontieu, B. 2009, ApJL, 702, L168
Flint, C., Vahala, G., Vahala, L., & Soe, M. 2014, REDS, 170, 429
Fontela, J. M., Avrett, E. H., & Loeser, R. 1990, ApJ, 355, 700
Galsgaard, K., Archontis, V., Moreno-Insertis, F., & Hood, A. W. 2007, ApJ, 666, 516
González-Avilés, J. J., Cruz-Osorio, A., Lora-Clavijo, F. D., & Guzmán, F. S. 2015, MNRAS, 454, 1871
González-Avilés, J. J., & Guzmán, F. S. 2015, MNRAS, 451, 4819
Goodman, M. L. 2012, ApJ, 757, 188
Griffiths, N. W., Fisher, G. H., Woods, D. T., & Siegmund, H. W. , 1999, ApJ, 512, 992
Hansteen, V. H., De Pontieu, B., Ruoppe van der Voort, L., van Noort, M., & Carlsson, M. 2006, ApJL, 647, L73
He, J., Marsch, E., Tu, C., & Tian, H. 2009, ApJL, 705, L217
Heggland, L., De Pontieu, B., & Hansteen, V. H. 2007, ApJ, 666, 1227
Heggland, L., De Pontieu, B., & Hansteen, V. H. 2009, ApJ, 702, 1
Isobe, H., Proctor, M. R. E., & Weiss, N. O. 2008, ApJL, 679, L57
Jiang, R. L., Fang, C., & Chen, P. F. 2012, CoPhC, 183, 1617
Judge, P. G., Tritschler, A., & Chye Low, B. 2011, ApJL, 730, L4
Kosugi, T., Matsuzaki, K., Sakao, T., et al. 2007, SoPh, 243, 3
Kuridze, D., Morton, R. J., Erdélyi, R., et al. 2012, ApJ, 750, 51
Kuridze, D., Zaqarashvili, T. V., Henriques, V., et al. 2016, arXiv:1608.01497
Langangen, Ø., De Pontieu, B., Carlsson, M., et al. 2008, ApJL, 679, L167
LeVeque, R. J. 1992, Numerical Methods for Conservations Laws (Basel: Birkhäuser)
Li, S. 2005, JCoPh, 203, 344
Mariska, J. T. 1992, The Solar Transition Region (Cambridge: Cambridge Univ. Press)
Martínez-Sykora, J., Hansteen, V., De Pontieu, B., & Carlsson, M. 2009, ApJ, 701, 1569
Martínez-Sykora, J., Hansteen, V., & Moreno-Insertis, F. 2011, ApJ, 736, 9
Matsumoto, T., & Shibata, K. 2010, ApJ, 710, 1857
McIntosh, S. W., Davey, A. R., Hassler, D. M., et al. 2007, ApJ, 654, 650
McIntosh, S. W., de Pontieu, B., Carlsson, M., et al. 2011, Natur, 475, 477
McLaughlin, J. A., Verth, G., Fedun, V., & Erdélyi, R. 2012, ApJ, 749, 30
Murawski, K., Srivastava, A. K., & Zaqarashvili, T. V. 2011, A&A, 535, A58
Murawski, K., & Zaqarashvili, T. V. 2010, A&A, 519, A8
Narang, N., Arbacher, R. T., Tian, H., et al. 2016, SoPh, 291, 1129
Nishizuka, N., Nakamura, T., Kawate, T., Singh, K. A. P., & Shibata, K. 2011, ApJ, 731, 43
Nishizuka, N., Shimizu, M., Nakamura, T., et al. 2008, ApJL, 683, L83
Okamoto, T. J., & De Pontieu, B. 2011, ApJL, 736, L24
Pariat, E., Antiochos, S. K., & DeVore, R. C. 2009, ApJ, 691, 61
Pariat, E., Antiochos, S. K., & DeVore, C. R. 2010, ApJ, 714, 1762
Pariat, E., Dalmasse, K., DeVore, C. R., & Karpen, J. 2015, A&A, 573, 15
Priest, E. R. 1982, Solar Magnetohydrodynamics (Dordrecht: Reidel)
Priest, E. R. 1984, Solar Magnetohydrodynamics (Berlin: Springer)
Priest, E. R. 2014, Magnetohydrodynamics of the Sun (Cambridge: Cambridge Univ. Press), doi:10.1017/CBO9781139020732
Priest, E. R., Forbes, T., & Murdin, P. 2000, Magnetic Reconnection: MHD Theory and Applications (Cambridge: Cambridge Univ. Press)
Rachmeler, L., Pariat, E., DeForest, C., & Antiochos, S. K. 2010, ApJ, 715, 1556
Rouppe van der Voort, L., Leenaarts, J., de Pontieu, B., Carlsson, M., & Vissers, G. 2009, ApJ, 705, 272
Scharmer, G. B., Narayan, G., Hillberg, T., et al. 2008, ApJL, 689, L69
Scullion, E., Erdélyi, R., Fedun, V., & Doyle, J. G. 2011, ApJ, 743, 14
Shibata, K., Nishikawa, T., Kitai, R., & Suematsu, Y. 1982, SoPh, 77, 121
Shibata, K., & Suematsu, Y. 1982, SoPh, 78, 333
Shibata, K., Nakamura, T., Matsumoto, T., et al. 2007, Sci, 318, 5836
Shu, C. W., & Osher, S. J. 1989, JCoPh, 83, 32
Singh, K. A., Shibata, K., Nishizuka, N., & Isobe, H. 2011, PhPl, 18, 111210
Singh, K. A. P., Isobe, H., Nishizuka, N., Nishida, K., & Shibata, K. 2012, ApJ, 759, 33
Skogsrud, H., Rouppe Van Der Voort, L., De Pontieu, B., & Pereira, T. M. 2015, ApJ, 806, 170
Sterling, A. C., & Moore, R. L. 2016, ApJL, 828, 1

Su, Y., Veronig, A. M., Holman, G. D., et al. 2013, NatPh, 9, 489
Suematsu, Y., Wangm, H., & Zirin, H. 1995, ApJ, 450, 411
Takasao, A., Asai, A., Isobe, H., & Shibata, K. 2012, ApJL, 745, L6
Tavabi, E., Koutchmy, S., Ajabshirizadeh, A., Ahangarzadeh Maralani, A. R., & Zeighmani, S. 2015, A&A, 573, A4
Tavabi, E., Koutchmy, S., & Golub, L. 2015, SoPh, 290, 2871
Tomczyk, S., McIntosh, S. W., Keil, S. L., et al. 2007, Sci, 317, 1192
Toro, E. F. 2009, Riemann Solvers and Numerical Methods for Fluid Dynamics (Berlin: Springer)
Tsiropoula, G., Tziotziou, K., Kontogiannis, I., et al. 2012, SSRv, 169 181
Wang, J., Li, W., Denker, C., et al. 2000, ApJ, 530, 1071
Wilhelm, K. 2000, A&A, 360, 351
Yokoyama, T., & Shibata, K. 1995, Natur, 375, 42
Yokoyama, T., & Shibata, K. 1996, PASJ, 48, 353
Zaqarashvili, T. V., & Erdélyi, R. 2009, SSRv, 149, 355
Zaqarashvili, T. V., Vörös, Z., & Zhelyazkov, I. 2014, A&A, 561, A62
Zhang, Y. Z., Shibata, K., Wang, J. X., et al. 2012, ApJ, 750, 16